# Finite element formulation for compressible multiphase flows and its application to pyroclastic gravity currents

Andrea Montanino[1,2], Alessandro Franci[3,4], Riccardo Rossi[3,4], Giulio Zuccaro[1,2]

[1] *Department of Structures for Engineering and Architecture*
*University of Naples "Federico II"*
*Via Claudio 21, 80125, Naples (ITALY)*
[2] *PLINIVS - LUPT Study Centre*
*University of Naples "Federico II"*
*Via Toledo 402, 80134, Naples (ITALY)*
[3] *International Centre for Numerical Methods in Engineering (CIMNE)*
*Av. Gran Capità, Barcelona (SPAIN)*
[4] *Universitat Politécnica de Catalunya (UPC)*
*Carrer de Jordi Girona, 31, Barcelona (SPAIN)*

**Abstract**

The numerical modeling of compressible multiphase flows is of high interest for several engineering applications. In this work, we focus on the study of pyroclastic flows arising from volcanic eruptive events. An accurate evaluation of the effects of this multiphase flow is of crucial importance for the Civil Protection for the preservation of urban settlements in volcanic areas. In this work, we propose a Finite Element formulation for the simulation of pyroclastic flows at conditions of thermal and kinetic equilibrium. This analysis belongs to the class of advection dominated problems, which are known to suffer from numerical instabilities. The required stabilization is provided by using a Variational Multiscale Method, typically used for monophase compressible flows and extended here for the first time to multiphase flows. The stabilized formulation is validated with benchmark problems for compressible flows, which are solved for both monophase and multiphase cases. A throughout comparison of the numerical results of the two different flows is also presented. Moreover, the numerical formulation is applied to the simulation of representative cases of pyroclastic flows considering large-scale computational domains and realistic material properties and initial thermal-kinematic conditions. The numerical analyses presented show the accuracy of the proposed method for the simulation of compressible multiphase flows and its suitability for risk assessment studies of urban settlements prone to be affected by pyroclastic gravity currents.

*Keywords:* Multiphase flows, pyroclastic flows, Variational Multiscale stabilization

---

## 1. Introduction

The numerical simulation of compressible multiphase flows is a topic of great relevance for multiple engineering applications, such as air pollution dispersion, transport phenomena, particulate flows, and the dynamic of non-mixable fluids.

Another application of interest is the simulation of pyroclastic flows originated from explosive eruptive events. Pyroclastic flows consist of a dilute mixture of gases and solid particulate [1, 2] and their study is of particular relevance for institutions of Civil Protection, which need to quantify the risk associated with volcanic eruptive events, assess the vulnerability of the built environment [3, 4], design the emergency plans [5], and implement the best engineering countermeasures (including the design of *ad hoc* systems for building protection, such as panels and resistant fixtures [6]). For a correct realization of these tasks, it is of paramount importance to value accurately the potential effects of pyroclastic flows on the urban environment and estimate quantities of interest, such as the pressure and temperature values acting on civil structures and infrastructures [7].

The numerical simulation of pyroclastic volcanic eruptions has been generally focused on the phenomena occurring at the volcano level. Different numerical approaches and formulations have been proposed in the literature for this specific objective. Fundamentals about the description of multiphase flows can be found in [8]. Following this work, in [9, 10] the conservation laws are written in terms of densities, velocity, enthalpy, and pressure, using implicit solvers to couple the different variables through the equation of state. On the other hand, in [11] the same problem is approached in terms of conservative variables (density, momentum and total energy).

Differently from the mentioned works, here we focus on the study of pyroclastic flows at the scale of the urban settlements [12]. In particular, we analyze the effect of the pyroclastic flow at a distance from the volcano such that the condition of thermal and kinetic equilibrium can be assumed

[13, 14, 15]. This hypothesis allows us to reduce the number of unknown variables and to neglect the terms related to the drag and heat transfer between different phases of the mixture.

The resulting set of governing equations has formal similarity with the case of the compressible monophase flow. It is well known that the finite element solution of this kind of problem leads to numerical instabilities due to the dominance of the convective term [16, 17, 18]. In the literature, several stabilization methods for advection dominant problems have been proposed, basing either on algebraic arguments, such as in [19, 20, 21], or on the incapacity of the Finite Element Method (FEM) to represent phenomena at a smaller scale than the discretization size. The latter is the case of the Variational Multiscale (VMS) technique [22], which separates variables and test functions on the part that can be represented at the finite elements scale and the remainder that has to be suitably approximated. The VMS stabilization method has been applied to different kinds of analyses, such as advection-diffusion-reaction problems [23], incompressible [24, 25] and compressible Navier-Stokes equations [26, 27, 28], and Burger's equation [29]. Nevertheless, to the best of the Authors' knowledge, so far the VMS method has been applied only to compressible monophase flows. In this work, we extend its application to compressible multiphase flows, *i.e.* dilute gas-solid mixtures.

Among the large variety of stabilization methods introduced in the framework of the VMS techniques, we use here the quasi-static Algebraic-Sub Grid Scales (ASGS, see [30]), leaving the development of different VMS stabilization methods for future work.

In order to deal with the shock waves that may appear in compressible flows at the supersonic regime and to avoid undesired nonphysical oscillations of the FEM solution across discontinuities, the numerical method is also provided with a shock-capturing technique. To this end, the method proposed by [31] for monophase problems and also used in [32, 33], is here extended to the multiphase case.

Concerning the time marching scheme, considering the high non-linearity of the problem and the need for a fast and robust algorithm for large-scale computations, an explicit approach was considered preferable to an implicit one. This allows to avoid problems of convergence, to limit the memory occupation, and to ease the code parallelization. These features are of crucial importance to enable the solution of large-scale problems, as those addressed in this work.

Several numerical examples are presented to show the validity of the method and its suitability for risk assessment studies of urban settlements potentially affected by pyroclastic flows. In particular, first, we analyze accuracy, convergence and robustness of the stabilized method in the solution of benchmark problems for compressible flows, both in supersonic and subsonic regimes and for both monophase and multiphase flows. Then, we apply the proposed method to the simulation of two representative problems of pyroclastic gravity currents impacting against civil constructions. In one of these tests, we consider a large scale three-dimensional geometry and realistic material properties and boundary conditions, mimicking an actual pyroclastic flow scenario. A quantitative estimation of the damages produced by the pyroclastic flow over the civil constructions is also given, basing on the criteria for damages estimation provided in [4].

We also remark that, given the lack of reference solutions for compressible multiphase analysis, the present work also provides benchmark cases solutions that can be useful for comparison purposes with other numerical strategies.

The paper is organized as follows. In Section 2, we introduce the governing equations, specifying the hypotheses at the base of the formulation. In Section 3, we derive the stabilized finite element method used for the multiphase compressible flows. Specifically, in Section 3.1, we derive the weak form, in Section 3.2, we extend the application of the VMS stabilization method to the case of multiphase flows, in Section 3.3, we present the adopted shock-capturing technique, and finally, in Section 3.4, we derive the fully discretized form of the problem. Section 4 is fully devoted to present the numerical examples solved with the proposed formulation. Finally, in Section 5, we discuss the results obtained and highlight the main contributions of the work.

## 2. Governing equations

The dynamic of multiphase flows is described by the equations of conservation of mass, linear momentum, and total energy. In this work, we focus on the study of a two-phase mixture with one gas and one solid phase.

Following [11], the dynamic of the gas phase is described as

$$\frac{\partial}{\partial t}(\varepsilon_g \rho_g) + \frac{\partial}{\partial x_i}(\varepsilon_g \rho_g u_{g,i}) = 0 \tag{1a}$$

$$\frac{\partial}{\partial t}(\varepsilon_g\rho_g u_{g,i})+\frac{\partial}{\partial x_j}(\varepsilon_g\rho_g u_{g,i}u_{g,j}+\varepsilon_g p_g) = p_g\frac{\partial\varepsilon_g}{\partial x_i}+\frac{\partial\tau_{g,ij}}{\partial x_j}+\varepsilon_g\rho_g b_{g,i}-D(u_{g,i}-u_{s,i}) \tag{1b}$$

$$\begin{aligned}\frac{\partial}{\partial t}(\varepsilon_g\rho_g e_g) + \frac{\partial}{\partial x_i}((\varepsilon_g\rho_g e_g + \varepsilon_g p_g)u_{g,i}) = -p_g\frac{\partial}{\partial x_i}(\varepsilon_s u_{s,i}) + u_{g,i}\frac{\partial}{\partial x_j}\tau_{g,ij}\\ -\frac{\partial}{\partial x_i}q_{g,i} + \varepsilon_g\rho_g b_{g,i}u_{g,i} + \varepsilon_g\rho_g r_g - D(u_{g,i}-u_{s,i})u_{g,i} - Q(T_g - T_s)\end{aligned} \tag{1c}$$

where $t$ is the time, $x_i$ are the spatial coordinates, $\varepsilon_g$ and $\varepsilon_s$ are the phase concentrations for the gas and the solid phase, respectively, being $\varepsilon_g+\varepsilon_s = 1$, $\rho_g$ is the gas density, $\mathbf{u}_g$ and $\mathbf{u}_s$ are the velocities of the gas and solid phases, respectively, $p_g$ is the thermodynamic pressure of the gas phase, $e_g$ is the specific energy of the gas phase, $T_g$ and $T_s$ are the temperatures of the two phases, $\boldsymbol{\tau}_g$ and $\mathbf{q}_g$ are the stress tensor and the heat flow vector in the gas phase, respectively, $\mathbf{b}_g$ and $r_g$ are the body force and the heat source for the gas phase, respectively. Finally, $D(u_{g,i}-u_{s,i})$ and $Q(T_g-T_s)$ are dissipative terms that account for momentum and energy exchanges between the two phases.

Similarly, the equations of conservation for the solid phase read

$$\frac{\partial}{\partial t}(\varepsilon_s\rho_s) + \frac{\partial}{\partial x_i}(\varepsilon_s\rho_s u_{s,i}) = 0 \tag{2a}$$

$$\frac{\partial}{\partial t}(\varepsilon_s\rho_s u_{s,i})+\frac{\partial}{\partial x_j}(\varepsilon_s\rho_s u_{s,i}u_{s,j}) = -\varepsilon_s\frac{\partial p_g}{\partial x_i}+\frac{\partial\tau_{s,ij}}{\partial x_j}+\varepsilon_s\rho_s b_{s,i}+D(u_{g,i}-u_{s,i}) \tag{2b}$$

$$\begin{aligned}\frac{\partial}{\partial t}(\varepsilon_s\rho_s e_s) + \frac{\partial}{\partial x_i}(\varepsilon_s\rho_s e_s u_{s,i}) = -\varepsilon_s u_{s,i}\frac{\partial p_g}{\partial x_i} + u_{s,i}\frac{\partial}{\partial x_j}\tau_{s,ij}\\ -\frac{\partial}{\partial x_i}q_{s,i} + \varepsilon_s\rho_s b_{s,i}u_{s,i} + \varepsilon_s\rho_s r_s + D(u_{g,i}-u_{s,i})u_{s,i} + Q(T_g - T_s)\end{aligned} \tag{2c}$$

In Equations (2), $\rho_s$ is the density of the solid phase, $e_s$ is the specific energy of the solid phase, $\boldsymbol{\tau}_s$ and $\mathbf{q}_s$ are the stress tensor and the heat flow vector in the solid phase, respectively, $\mathbf{b}_s$ is the vector of body forces applied on the solid phase, and $r_s$ are energy sources due to the solid phase.

The energy terms $e_g$ and $e_s$ comprise a thermal and a kinetic contribution and are computed as

$$e_g = c_v T_g + \frac{1}{2} u_{g,i} u_{g,i} \tag{3a}$$

$$e_s = c_s T_s + \frac{1}{2} u_{s,i} u_{s,i} \tag{3b}$$

where $c_v$ is the specific heat at constant volume of the gas, and $c_s$ is the specific heat of the solid material.

Problems (1)-(2) are closed by the equation of state for ideal gases, that reads

$$p_g = \rho_g R T_g \tag{4}$$

being $R$ the specific constant of the gas, and by the incompressibility of the solid particles, expressed by $\rho_s = const$.

We highlight that system (1)-(2) can be considered as a particular case of the Baer-Nunziato [34, 35, 36, 37, 38, 39, 40] (or Saurel-Abgrall [41]) model, which holds also for high values of phase concentrations or concentration gradients. On the other hand, our approach considers extremely dilute mixtures, where the solid concentration is limited, *i.e.*, $\varepsilon_s < 10^{-2}$. Under these conditions, the Baer-Nunziato model can be simplified as system (1)-(2). Furthermore, for such dilute mixtures, the terms $p_g \partial \varepsilon_g / \partial x_i$ and $-p_g \partial(\varepsilon_s u_{s,i})/\partial x_i$ of Equations (1), and the terms $-\varepsilon_s \partial p_g / \partial x_i$ and $-\varepsilon_s u_{s,i} \partial p_g / \partial x_i$ of Equations (2) can be dropped, and the total pressure can be defined as $p = \varepsilon_g p_g$ [11]. Therefore, Equations (1) and (2) can be simplified into

$$\frac{\partial}{\partial t}(\varepsilon_g \rho_g) + \frac{\partial}{\partial x_i}(\varepsilon_g \rho_g u_{g,i}) = 0 \tag{5a}$$

$$\frac{\partial}{\partial t}(\varepsilon_g \rho_g u_{g,i}) + \frac{\partial}{\partial x_j}(\varepsilon_g \rho_g u_{g,i} u_{g,j} + p) = \frac{\partial \tau_{g,ij}}{\partial x_j} + \varepsilon_g \rho_g b_{g,i} - D(u_{g,i} - u_{s,i}) \tag{5b}$$

$$\begin{aligned} \frac{\partial}{\partial t}(\varepsilon_g \rho_g e_g) + \frac{\partial}{\partial x_i}((\varepsilon_g \rho_g e_g + p) u_{g,i}) = u_{g,i} \frac{\partial}{\partial x_j} \tau_{g,ij} - \frac{\partial}{\partial x_i} q_{g,i} + \\ \varepsilon_g \rho_g b_{g,i} u_{g,i} + \varepsilon_g \rho_g r_g - D(u_{g,i} - u_{s,i}) u_{g,i} - Q(T_g - T_s) \end{aligned} \tag{5c}$$

$$\frac{\partial}{\partial t}(\varepsilon_s \rho_s) + \frac{\partial}{\partial x_i}(\varepsilon_s \rho_s u_{s,i}) = 0 \tag{5d}$$

$$\frac{\partial}{\partial t}(\varepsilon_s \rho_s u_{s,i}) + \frac{\partial}{\partial x_j}(\varepsilon_s \rho_s u_{s,i} u_{s,j}) = \frac{\partial \tau_{s,ij}}{\partial x_j} + \varepsilon_s \rho_s b_{s,i} + D(u_{g,i} - u_{s,i}) \tag{5e}$$

$$\frac{\partial}{\partial t}(\varepsilon_s \rho_s e_s) + \frac{\partial}{\partial x_i}(\varepsilon_s \rho_s e_s u_{s,i}) = u_{s,i}\frac{\partial}{\partial x_j}\tau_{s,ij} - \frac{\partial}{\partial x_i}q_{s,i} + \varepsilon_s \rho_s b_{s,i} u_{s,i} + \varepsilon_s \rho_s r_s + D(u_{g,i} - u_{s,i})u_{s,i} + Q(T_g - T_s) \tag{5f}$$

### *2.1. Multiphase flows in thermal and kinetic equilibrium*

Equations (5) are explicitly coupled by the dissipative terms $D(u_{g,i}-u_{s,i})$ and $Q(T_g - T_s)$ that vanish when the velocities and the temperatures of the two phases are the same. The effect of both dissipative terms is to homogenize the temperature and velocity fields: the time and space needed for reaching this effect depend on the characteristics of the flow and the size of the particles [9, 42, 43]. In particular, a particle of mass $m$ and radius $\sigma$, inserted in a flow with velocity $v$, adapts to the fluid velocity in a time

$$\tau_u = \frac{m}{6\pi\sigma\mu_g} \tag{6}$$

where $\mu_g$ is the viscosity of the gas [42]. Similarly, the time needed for a particle at a temperature $T_p$ to adapt to the flow temperature $T_f$ is

$$\tau_T = \frac{mc_p}{4\pi\sigma\lambda_g} \tag{7}$$

being $c_p$ the specific heat at constant pressure of the gas, and $\lambda_g$ is the thermal diffusivity [42].

When $t > \tau_u$ and $t > \tau_T$, we can consider that the condition of thermal and kinetic equilibrium is fulfilled [15, 42]. In this situation, the solid and the gas phases are assumed to have the same velocity and temperature fields. This hypothesis allows us to set $\mathbf{u}_g = \mathbf{u}_s = \mathbf{u}$ and $T_g = T_s = T$ in Equations (5). Using this and summing up the equations of conservation of mass, momentum, and total energy of the two phases (Eq. 5), we obtain the following compact form of the conservation equations for the solid-gas mixture

$$\frac{\partial}{\partial t}\rho + \frac{\partial}{\partial x_i}(\rho u_i) = 0 \tag{8a}$$

$$\frac{\partial}{\partial t}(\rho u_i) + \frac{\partial}{\partial x_j}(\rho u_i u_j + p) = \frac{\partial \tau_{ij}}{\partial x_j} + \rho b_i \tag{8b}$$

$$\frac{\partial}{\partial t}E + \frac{\partial}{\partial x_i}((E+p)u_i) = u_i\frac{\partial}{\partial x_j}\tau_{ij} - \frac{\partial}{\partial x_i}q_i + \rho b_i u_i + \rho r \tag{8c}$$

where we can recognize the mixture mass conservation equation (Eq. (8a)), the mixture momentum conservation equation (Eq. (8b)), and the the mixture energy conservation equation (Eq. (8c)). Finally, the mass conservation of the solid phase is guaranteed by retaining Equation (5d), which is rewritten in terms of the mixture velocity as

$$\frac{\partial}{\partial t}(\varepsilon_s\rho_s) + \frac{\partial}{\partial x_i}(\varepsilon_s\rho_s u_i) = 0 \tag{9}$$

In Equations (8)-(9), $\rho = \varepsilon_g\rho_g + \varepsilon_s\rho_s$ is the total density of the mixture, $E = \varepsilon_g\rho_g e_g + \varepsilon_s\rho_s e_s$ is the total energy of the mixture, $\boldsymbol{\tau}$ and $\mathbf{q}$ are suitable compositions of the stress tensors and the heat flows of the components of the mixture, and $\mathbf{b}$ and $r$ are source terms.

The viscous term of the mixture is assumed as the usual one adopted for Newtonian fluids [42], that is

$$\tau_{ij} = \mu_m\left[\left(\frac{\partial u_i}{\partial x_j} + \frac{\partial u_j}{\partial x_i}\right) - \frac{2}{3}\frac{\partial u_k}{\partial x_k}\delta_{ij}\right] \tag{10}$$

where the mixture dynamic viscosity $\mu_m$ is computed as [42]

$$\mu_m = \frac{\mu_g}{1+\kappa} \tag{11}$$

being $\mu_g$ the dynamic viscosity of the gas, and

$$\kappa = \frac{\varepsilon_s\rho_s}{\varepsilon_g\rho_g} \tag{12}$$

It is worth remarking that, since $\kappa > 0$, the equivalent viscosity of a multiphase flow is lower than the one in a monophase case. As a consequence, for the same velocity field, a multiphase analysis is expected to have a higher Reynolds number than the respective monophase problem and turbulent phenomena are expected to appear earlier.

Similarly, the heat flux for the mixture is written according to the Fourier law, as $q_i = -\lambda_m\partial T/\partial x_i$, being $\lambda_m$ the mixture thermal diffusivity expressed as

$$\lambda_m = \frac{\lambda_g}{1+\kappa} \tag{13}$$

where $\lambda_g$ is the thermal diffusivity of the gas.

### *2.2. Conservative form*

For the explicit solution of problem (8)-(9) it is convenient to write all equations in terms of a set of conservative variables as

$$\frac{\partial}{\partial t}\mathbf{U} + \frac{\partial}{\partial x_i}\mathbf{F}_i = \frac{\partial}{\partial x_i}\mathbf{G}_i + \mathbf{S} \tag{14}$$

where $\mathbf{U}$ is the set of conservative variables, $\mathbf{F}$ is the matrix of the convective flux, $\mathbf{G}$ is the dissipative flux, and $\mathbf{S}$ is the source term.

For a two-phase mixture, the vector of conservative variables is

$$\mathbf{U} = [\rho, P_s, M_i, E]^T \tag{15}$$

where $P_s = \varepsilon_s \rho_s$ is the contribution of the solid part to the total density of the mixture, and $M_i = \rho u_i$ is the linear momentum of the mixture. The corresponding convective and dissipative fluxes are then

$$\mathbf{F} = \begin{bmatrix} M_j \\ \dfrac{P_s}{\rho} M_j \\ M_i \dfrac{M_j}{\rho} + p\delta_{ij} \\ \dfrac{M_j}{\rho}(E+p) \end{bmatrix} \quad , \quad \mathbf{G} = \begin{bmatrix} 0_j \\ 0_j \\ \tau_{ij} \\ u_i \tau_{ij} + q_j \end{bmatrix} \tag{16}$$

where $\delta_{ij}$ is the Kronecker delta. The variable $p$ can be expressed in terms of the conservative variables as

$$p = \frac{R(\rho - P_s)}{c_m} \left( E - \frac{1}{2} \frac{M_i M_i}{\rho} \right) \tag{17}$$

where

$$c_m = P_s c_s + (\rho - P_s) c_v \tag{18}$$

is the specific heat of the mixture. Finally, the source vector is

$$\mathbf{S} = [0, 0, \rho b_i, M_j b_j + \rho r]^T \tag{19}$$

that can be conveniently written as $\mathbf{S} = \mathbf{T}\mathbf{U}$, where

$$\mathbf{T} = \begin{bmatrix} 0 & 0 & 0_j & 0 \\ 0 & 0 & 0_j & 0 \\ b_i & 0_i & 0_{ij} & 0_i \\ r & 0 & b_j & 0 \end{bmatrix} \tag{20}$$

Other fields of interest can be retrieved from the conservative variables. Among them we mention the temperature

$$T = \frac{p}{\rho_g R} = \frac{1}{c_m}\left(E - \frac{1}{2}\frac{M_i M_i}{\rho}\right) \tag{21}$$

and the speed of sound (expressed as [11])

$$a_m = a_g \sqrt{\frac{\rho_g}{\gamma \varepsilon_g \rho}} \tag{22}$$

being $a_g$ the speed of sound in the monophase gas, and $\gamma$ the heat capacity ratio of the gas. For extremely dilute mixtures (*i.e.* $\varepsilon_g \simeq 1$), Equation (22) reduces to

$$a_m = a_g \sqrt{\frac{\rho - P_s}{\gamma \rho}} \tag{23}$$

It is interesting to notice that, since $\sqrt{(\rho - P_s)/\gamma\rho} < 1$, in dilute mixtures the speed of sound is lower than in monophase flows.

Another variable of interest is the Mach number $Ma = u/a$, which gives information about the compressibility regime of the mixture. It is worth noting that, for the same velocity field, a mixture flow has a higher Mach number with respect to the monophase flow, since the speed of sound is lower in mixture than in the monophase flow.

## 3. Stabilized FEM formulation

### *3.1. Weak form*

Using the Euler-Jacobian matrix $A_{ijk} = A_{ijk}(\mathbf{U}) = \dfrac{\partial F_{ij}}{\partial U_k}$, problem (14) is rewritten as

$$\frac{\partial U_i}{\partial t} + A_{ijk}\frac{\partial U_k}{\partial x_j} = \frac{\partial G_{ij}}{\partial x_j} + T_{ik}U_k \tag{24}$$

Let us consider a domain $\Omega \in \mathbb{R}^3$ and a discretization in a finite number of elements $\Omega_h$. Premultiplying Equation (24) by the test function vector $\mathbf{V}$ and integrating over $\Omega_h$, we get the weak form as

$$\left(V_i, \frac{\partial U_i}{\partial t}\right) + (V_i, L_{ik}U_k) - \left(V_i, \frac{\partial G_{ij}}{\partial x_j}\right) = 0 \qquad \forall V_i \in \mathbb{W} \tag{25}$$

where $\mathbb{W}$ is the space of the variables and the test functions. The non-linear operator $L_{ik}$ is defined as

$$L_{ik}(\mathbf{U}) = A_{ijk}(\mathbf{U})\frac{\partial}{\partial x_j} - T_{ik} \tag{26}$$

We remark that in Eq. 25 we have also introduced the notation $(a, b) = \int_{\Omega_h} ab d\Omega_h$.

### *3.2. Variational Multiscale stabilization*

It is well known that a standard Galerkin formulation for advection dominated problems suffers from instabilities that result in spurious numerical results [16, 17, 18].

In this work, we stabilize the numerical formulation using the Variational Multiscale Method [21, 22]. This stabilization procedure is designed to account for the effects of the subgrid scale, *i.e.* those effects that cannot be captured at the scale of the finite elements. This is achieved by splitting the space of the conservative variables and test functions as $\mathbb{W} = \mathbb{W}^h + \tilde{\mathbb{W}}$, being $\mathbb{W}^h$ the space of the functions that can be represented by standard finite elements, and $\tilde{\mathbb{W}}$ the space of the subscale.

Following the standards VMS technique, Equation (25) is therefore projected onto the spaces $W^h$ and $\tilde{\mathbb{W}}$, getting two different sets of equations

$$\left(V_i^h, \frac{\partial (U_i^h + \tilde{U}_i)}{\partial t}\right) + \left(V_i^h, L_{ik}(U_k^h + \tilde{U}_k)\right) - \left(V_i^h, \frac{\partial}{\partial x_j}G_{ij}(\mathbf{U}^h + \tilde{\mathbf{U}})\right) = 0, \quad \forall V^h \in \mathbb{W}^h \tag{27a}$$

$$\left(\tilde{V}_i, \frac{\partial(U_i^h + \tilde{U}_i)}{\partial t}\right) + \left(\tilde{V}_i, L_{ik}(U_k^h + \tilde{U}_k)\right) - \left(\tilde{V}_i, \frac{\partial}{\partial x_j} G_{ij}(\mathbf{U}^h + \tilde{\mathbf{U}})\right) = 0, \quad \forall \tilde{V} \in \tilde{W} \tag{27b}$$

*Finite element scale.* Let us focus before on Equation (27a) referring to the finite element scale. We separate the terms computed at the finite element scale from the ones computed at the subgrid scale, neglect the contribution of the time derivative of the subgrid scale $\partial \tilde{\mathbf{U}}/\partial t$ (hypothesis of quasi-static subscales [27]) as well as the contribution of the subscale to the dissipative term $\partial G_{ij}(\tilde{\mathbf{U}})/\partial x_j$, since it involves the calculation of higher order derivatives that vanish for linear elements. Therefore, we obtain

$$\left(V_i^h, \frac{\partial U_i^h}{\partial t}\right) + \left(V_i^h, L_{ik} U_k^h\right) + \left(V_i^h, L_{ik} \tilde{U}_k\right) - \left(V_i^h, \frac{\partial G_{ij}(\mathbf{U}^h)}{\partial x_j}\right) = 0\,, \quad \forall V^h \in \mathbb{W}^h \tag{28}$$

After integrating by parts the third term of Equation (28) and some algebra, we obtain

$$\left(V_i^h, \frac{\partial U_i^h}{\partial t} + L_{ik} U_k^h\right) - \left(L_k^*, \tilde{U}_k\right) + \left(\frac{\partial V_i^h}{\partial x_j}, G_{ij}(\mathbf{U}^h)\right) = 0\,, \quad \forall V^h \in \mathbb{W}^h \tag{29}$$

where

$$L_k^* = \frac{\partial V_i^h}{\partial x_j} A_{ijk} + V_i B_{ijkm} \frac{\partial U_m^h}{\partial x_j} - V_i T_{ik} \tag{30}$$

is the adjoint term, and

$$B_{ijkm} = \frac{\partial A_{ijk}}{\partial U_m^h} \tag{31}$$

Equation (29) contains all terms that can be computed at the finite element scale, with exception of the subgrid scale term $\tilde{U}$, that is obtained from Equation (27b).

*Subgrid scale.* Focusing now on the subgrid scale, Equation (27b) is rewritten neglecting the time variation of the subscale and its contribution to dissipation as

$$\left(\tilde{V}_i, L_{ik}\tilde{U}_k\right) = -\left(\tilde{V}_i, \frac{\partial U_i^h}{\partial t} + L_{ik}U_k^h\right), \quad \forall \tilde{V} \in \tilde{W} \tag{32}$$

One of the key points of the VMS technique is the choice of the approximation of the non-linear operator applied to $\tilde{\mathbf{U}}$. Following the standard VMS practice, we used

$$L_{ik}\tilde{U}_k = \tau_{ik}^{-1}(\mathbf{U})\tilde{U}_k \tag{33}$$

where $\boldsymbol{\tau}$ is a diagonal matrix that depend on the characteristics of the flow

$$\boldsymbol{\tau}^{-1} = \begin{bmatrix} \tau_\rho^{-1} & 0 & 0 & 0 \\ 0 & \tau_\rho^{-1} & 0 & 0 \\ 0 & 0 & \tau_M^{-1} & 0 \\ 0 & 0 & 0 & \tau_E^{-1} \end{bmatrix} \tag{34}$$

with

$$\tau_\rho^{-1} = c_2\frac{\|\mathbf{u}\| + c_m}{h}, \quad \tau_M^{-1} = c_1\frac{\nu}{h^2} + c_2\frac{\|\mathbf{u}\| + c_m}{h}, \quad \tau_E^{-1} = c_1\frac{\lambda_m}{\rho c_p h^2} + c_2\frac{\|\mathbf{u}\| + c}{h} \tag{35}$$

being $c_1$ and $c_2$ algorithmic constants (in this work, $c_1 = 4$ and $c_2 = 2$) and $h$ the characteristic length of the element.

The coefficients of $\boldsymbol{\tau}^{-1}$, proposed in [27] for a monophase compressible flow, are here adapted for multiphase flows replacing the gas constants with the parameters of the mixture. In particular, the speed of the sound $c$ is replaced with the speed of the sound of the mixture $c_m$, and the specific heat at constant pressure $c_p$ is replaced by the corresponding value of the mixture. Basing on [42], this leads to

$$c_{p,m} = \frac{c_{p,g} + \kappa c_s}{1 + \kappa} \tag{36}$$

To solve Equation (32) we also need to choose a proper space for the projection of the residuals. Following the algebraic subgrid scale projection (ASGS) [30], we project the adjoint term $L_k^*$ onto the space of the residuals, obtaining

$$\tau_{ij}^{-1}\tilde{U}_j = R_i^h \tag{37}$$

where $\mathbf{R}^h$ is the residual at the scale of the finite elements.

Introducing Equation (37) into Equation (29), we obtain

$$\left(V_i^h, \frac{\partial U_i}{\partial t} + L_{ik} U_k\right) - \left(L_k^*, \tau_{kj} R_j^h\right) + \left(\frac{\partial V_i^h}{\partial x_j}, G_{ij}(\mathbf{U}_h)\right) = 0 \tag{38}$$

where all terms are evaluated at the scale of the finite element.

### *3.3. Discontinuity capturing technique*

In presence of strong discontinuities in the unknown variable fields, the finite element solution can give rise to spurious oscillations across the discontinuity.

A commonly adopted technique for this issue is the discontinuity capturing technique [31, 32, 33]. This procedure is generally adopted for compressible flows in a supersonic regime, where shock waves are admitted. The method consists of increasing the viscosity and thermal diffusivity affecting the conservation equations of momentum and total energy, as follows

$$\boldsymbol{\tau}_{DC} = \left(1 + \frac{\rho \nu_{DC}}{\mu}\right) \mathbb{D} \boldsymbol{\tau} \tag{39a}$$

$$\mathbf{q}_{DC} = \left(1 + \frac{\rho c_v k_{DC}}{\lambda}\right) \mathbf{K} \mathbf{q} \tag{39b}$$

where $\boldsymbol{\tau}_{DC}$ and $\mathbf{q}_{DC}$ are the stress tensor and the heat flux after the inclusion of the numerical diffusivity, respectively, and $\mathbb{D}$ and $\mathbf{K}$ are fourth- and second-order tensors defining the eventual anisotropy of the residual-based shock capturing on the momentum and energy equations, respectively. Finally, the parameters $\nu_{DC}$ and $k_{DC}$ are computed as

$$\nu_{DC} = \frac{1}{2} h C_a \frac{\|R_M\|}{\|\nabla M_h\|} \qquad \text{if } \|\nabla M_h\| \neq 0, \qquad 0 \quad \text{otherwise} \tag{40a}$$

$$k_{DC} = \frac{1}{2} h C_a \frac{\|R_E\|}{\|\nabla E_h\|} \qquad \text{if } \|\nabla E_h\| \neq 0, \qquad 0 \quad \text{otherwise} \tag{40b}$$

where $R_M$ and $R_E$ are the residuals of the equations of the momentum and total energy, and $C_a$ is an algorithmic constant that regulates the intensity of the added numerical viscosity. More details about the isotropic and anisotropic shock capturing models are given in [29].

For multiphase flows, a discontinuity capturing technique is needed also for the equation of conservation of the mass of the solid phase, to prevent spurious oscillations that could give nonphysical values of $P_s$. Thus, following [44], we include the following diffusive term on the right-hand side of Equation (9)

$$P_{s,diff} = \nabla \cdot \left( \frac{1}{2} h C_P \frac{R_P}{\|\nabla P_{s,h}\|} \mathbf{D} \nabla P_s \right) \quad \text{if } \|\nabla P_{s,h}\| \neq 0, \quad 0 \quad \text{otherwise} \tag{41}$$

where $C_P$ is the algorithmic constant and, in analogy with Equations (40), $R_P$ is the residual of the equation of conservation of the mass of the solid phase at the finite element scale. Here we have also introduced the second-order tensor

$$\mathbf{D} = \alpha_a \mathbf{a} \otimes \mathbf{a} + \alpha_c (\mathbf{I} - \mathbf{a} \otimes \mathbf{a}) \tag{42}$$

that regulates the anisotropy of the diffusivity on the solid phase transport equation, being $\mathbf{a}$ the unit vector in the direction of the flow. $\alpha_a$ and $\alpha_c$ are algorithmic constants. When $\alpha_a = \alpha_c$ a isotropic diffusivity is obtained, whereas the anisotropic one arises for $\alpha_a \neq \alpha_c$.

In the numerical tests presented in this work, we always consider isotropic shock-capturing. For all numerical examples, we set $C_a = 0.5$; for monophase cases, the constant $C_p$ is set to 0.0, whereas for multiphase cases we set $C_p = 0.5$.

### *3.4. Space and time discretization*

Equation (38) is discretized over a simplicial finite element mesh. On each element, the test functions and the unknowns are computed as

$$V_i^h = N_{ip} \hat{V}_p^h, \quad U_k^h = N_{kp} \hat{U}_p^h \tag{43}$$

being $\mathbf{N}$ the matrix of the linear shape functions.

After some algebra (whose details are illustrated in Appendix A), we get to the semi-discrete form

$$\frac{\partial}{\partial t} \hat{U}_i^h = \frac{\hat{F}_i(\mathbf{U}, t)}{m_i} \tag{44}$$

where $\hat{U}_i^h$ is the vector of nodal values of the conservative variables, $\hat{F}_i(\mathbf{U}, t)$ is the vector of nodal forces, and $m_i$ is the nodal mass, computed after lumping of the consistent mass matrix. The expression of these terms is reported in the Appendix A.

Using an explicit first-order Euler algorithm for the time integration of Equation (44), we obtain

$$\hat{U}_i^{h,n+1} = \hat{U}_i^{h,n} + \frac{\Delta t}{m_i}\hat{F}_i(\mathbf{U}^{h,n}, t^n) \tag{45}$$

where $n$ is the time step number and $\Delta t$ is the time step increment that is limited by the following CFL condition

$$\Delta t < \frac{h}{u + c} \tag{46}$$

In this work, we adopted an explicit method for its better performances for large scale computations. We remark that this a key skill for the analysis of real-world problems of pyroclastic flows. Computational cost reasons are also behind our choice of a first order Euler scheme instead of other linear multi-step explicit methods of higher order accuracy (*e.g.* Runge-Kutta methods) that would require multiple computations of the nodal residuals at each time step.

The implementation of the whole stabilized finite element method has been carried on in Kratos Multiphysics [45], an open-source coding environment for multiphysics applications.

## 4. Applications

In this section, we present several numerical tests to validate the proposed formulation for compressible multiphase flows. Before approaching multiphase analyses, we assess the accuracy and convergence of the formulation for the monophase case by solving some well-known benchmark problems, such as the Taylor-Green vortex problem [46], the monophase Sod tube [47], and a subsonic flow around a cylinder [27]. Some of these tests are then solved again considering multiphase flows to prove the robustness of the algorithm, confirm its convergent behavior, and assess its validity for multiphase analyses. In all multiphase examples, we assume that the hypothesis of kinetic and thermal equilibrium is already fulfilled at the beginning of the simulation. Finally, we analyze two cases of pyroclastic flows impacting civil buildings.

Again, the urban settlement is considered to be placed at a distance from the eruptive source such that the hypothesis of thermal and kinetic equilibrium is admissible. The first analysis is performed over a two dimensional domain and is presented to give an example of parametric study in the framework of pyroclastic gravity current, the second one is realized on a large-scale three-dimensional domain and is aimed at showing the applicability of the method to real-world pyroclastic flow problems.

In all the numerical tests, if not differently specified, the material parameters of the gas are $c_v = 722$ W/kg K, $c_p = 1010$ W/kg K, while, for the solid phase, we considered $\rho_s = 1800$ kg/m$^3$, and $c_s = 1300$ W/kg K.

### *4.1. The Taylor Green Vortex*

The Taylor Green vortex [46] is a well-assessed test in the framework of fluid dynamics analysis and is here studied to verify accuracy and robustness of the proposed numerical method. The problem consists in a square domain $(x, y) \in [0 \quad 2\pi] \times [0 \quad 2\pi]$ over which a smooth flow is induced by the following force term

$$\begin{aligned}
&b_x = \cos x \sin x (F(t))^2 - \cos y \sin x\,(2\mu F(t) + F'(t)) \\
&b_y = \sin y \cos y (F(t))^2 + \cos x\,(2\mu F(t) + F'(t)) \\
&r = 0
\end{aligned} \tag{47}$$

with $F(t) = 0.1\, t\, e^{-2\mu t}$ and $\mu = 0.1 kg/ms$.

A representation of the body forces at $t = 5$ s is given in Figure 1.

Slip conditions are imposed at the whole boundary of the domain and the initial conditions of the problem are

$$\begin{aligned}
&\rho(x, y, z, t) = 1 \\
&u_1(x, y, z, t) = 0 \\
&u_2(x, y, z, t) = 0 \\
&T(x, y, z, t) = 0.1
\end{aligned} \tag{48}$$

The analytical solution of the problem is

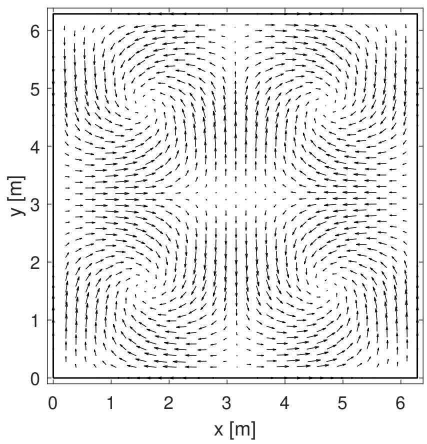


Figure 1: Taylor Green vortex problem: representation of the body forces

$$
\begin{aligned}
\rho(x, y, z, t) &= 1 \\
u_1(x, y, z, t) &= -\sin x \cos y \, F(t) \\
u_2(x, y, z, t) &= \cos x \sin y \, F(t) \\
T(x, y, z, t) &= 0.1
\end{aligned}
\tag{49}
$$

In Figure 2 we show the streamlines and velocity contours of the numerical solution.

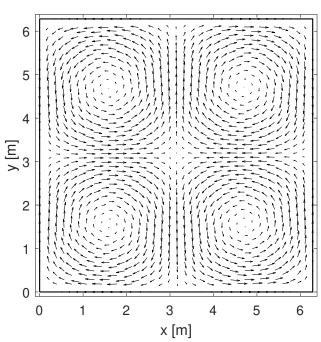


(a) Velocity streamlines

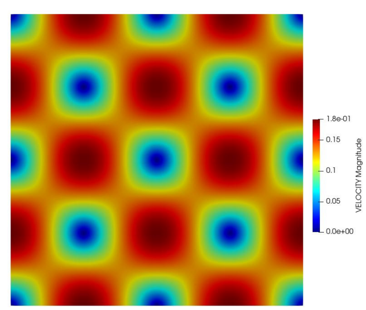


(b) Velocity magnitude

Figure 2: Taylor Green vortex problem. Streamlines and velocity contours.

The problem has been solved for five different finite element discretiza-

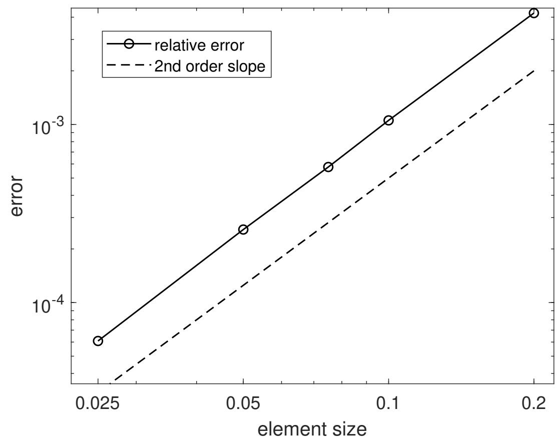


Figure 3: Taylor Green vortex problem: convergence diagram of the relative error for space discretization

tions ($h = 0.025m, 0.05m, 0.075m, 0.1m, 0.2m$) and time step sizes ($\Delta t = 2.5 \cdot 10^{-4}s,\ 5 \cdot 10^{-4}s,\ 10^{-3}s,\ 2.5 \cdot 10^{-3}s,\ 5 \cdot 10^{-3}s$). The L2 norm of the error with respect to the analytical solution has been evaluated at $t = 5s$, that is when $F(t)$ reaches its maximum value. The error measure has been computed as follows

$$err = \sqrt{\int_{\Omega} (sol_{an} - sol_{num})^2 d\Omega} \tag{50}$$

In Figure 3, we show the convergence diagram of the relative error versus the element characteristic length. As expected, the slope of the error curve is 2 in a logarithmic diagram.

In Figure 4, we show the convergence diagram of the relative error versus the time discretization. In accordance with forward Euler method theory, the error curve in a logarithmic diagram has a first order slope.

### *4.2. Sod shock tube*

The Sod shock tube [47] is another widely used benchmark for assessing the accuracy and robustness of numerical methods for the simulation of compressible flows in supersonic regime. Besides classical stabilized Eulerian finite elements [48], the Sod shock tube has been tackled using different numerical techniques, among which the Finite Volume Method [49, 50] and

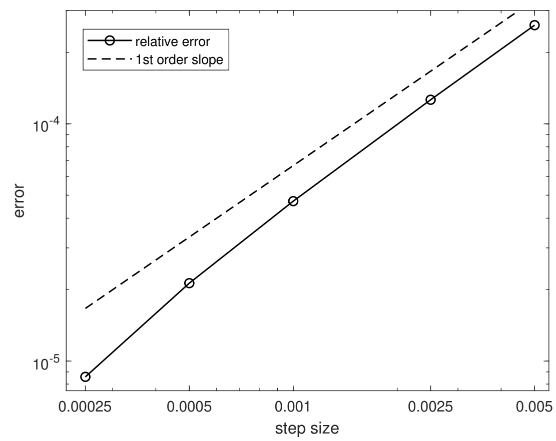


Figure 4: Taylor Green vortex problem: convergence diagram of the relative error for time discretization

the Particle Finite Element Method (PFEM) [51]. The problem consists in a one-dimensional domain of length $L = 1$ m, divided in two parts with different initial conditions: on the left side, $\rho_g = 1$ kg/m$^3$, $p = 1$ Pa, and $u = 0$ m/s; on the right side, $\rho_g = 0.125$ kg/m$^3$, $p = 0.1$ Pa, and $u = 0$ m/s.

The difference in pressure and density between the two parts of the domain gives rise to a shock wave. The analytical solution of this problem can be obtained via the iterative procedure detailed in [52].

The problem is here solved considering both a monophase flow, like in the original reference, and a two-phase one.

*Monophase case.* Figure 5 shows the pressure field obtained numerically at $t = 0.2$ s assuming $\varepsilon_s = 0$. The results are given for three different FEM meshes (*i.e.* 2168, 9062, and 56708 triangular elements), and are compared to the analytical solution. Also in this case, a very good agreement with the analytical solution and a clear convergent behavior are obtained. We also remark that, also for the coarser discretizations, the numerical solution of the three pressure plateaux is very well captured.

*Biphase case.* The same problem has been solved considering different initial solid particle concentrations in the domain. The initial gas density and pressure distributions are the same of the monophase case, whereas the initial solid concentration are $\varepsilon_s = 10^{-5}$, $\varepsilon_s = 10^{-4}$, and $\varepsilon_s = 10^{-3}$ for the three different examples.

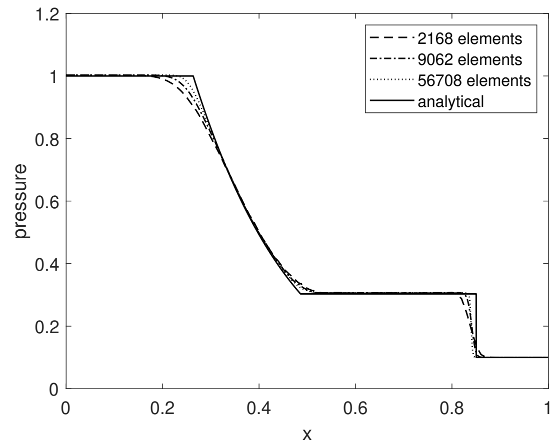


Figure 5: Monophase Sod shock tube problem: numerical and analytical solutions for different discretizations

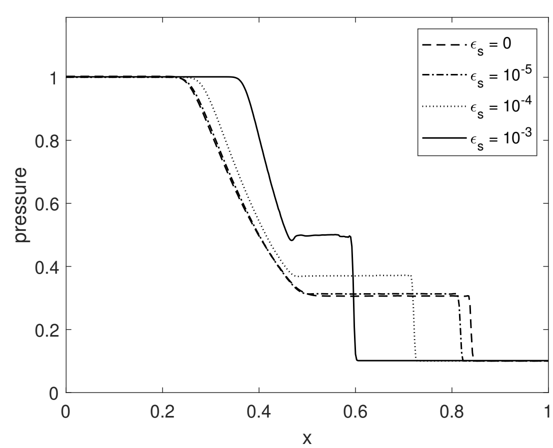


Figure 6: Biphase Sod shock tube problem: pressure diagram for different values of $\varepsilon_s$ with 56708 finite elements

Figure 6 plots the pressure solution obtained at $t = 0.2$ s for the three different solid concentrations.

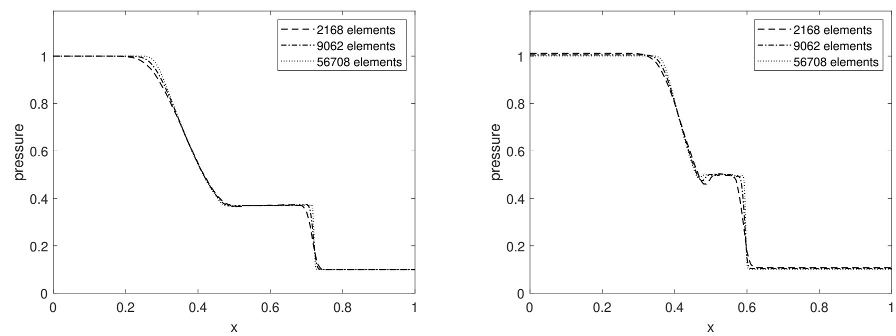


(a) $\varepsilon_s = 10^{-4}$ (b) $\varepsilon_s = 10^{-3}$

Figure 7: Biphase Sod shock tube problem: pressure diagram for different values of $\varepsilon_s$ and different discretizations

It is interesting to note that, for higher values of the solid concentration $\varepsilon_s$, due to the consequent decreasing of the speed of sound $c_m$ (Equation (22)), the pressure plateaux are preserved for a larger part. Furthermore, the graphs also show that, increasing $\varepsilon_s$, also the pressure value in the central part of the domain increases.

In Figures 7a and 7b, we show the pressure diagrams for the cases $\varepsilon_s = 10^{-4}$ and $\varepsilon_s = 10^{-3}$ for different discretizations. The graphs confirm the convergent behavior of the algorithm also for these multiphase analyses.

In Figure 8, we show the time evolution of the pressure for the cases $\varepsilon_s = 10^{-3}$ and $\varepsilon_s = 0$ from the beginning of the simulation until $t = 0.2$ s; it can be observed that, as expected, for the case $\varepsilon_s = 10^{-3}$ the speed of the sound is lower with respect to the monophase case.

### *4.3. Compressible flow around a cylinder*

This benchmark test consists of a compressible flow investing a cylinder of radius $r = 0.1$ m with a velocity of 1 m/s. When the flow is fully developed, an instability occurs behind the cylinder, generating a pattern of swirling vortices.

The domain and the dimensions of the problem are represented in Figure 9. As for the previous test, the problem is here solved considering both monophase and two-phase flows.

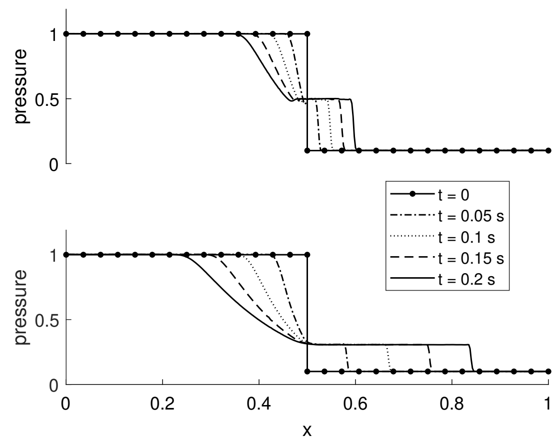


Figure 8: Biphase Sod shock tube problem: time evolution of the pressure for $\varepsilon_s = 10^{-3}$ (top) and $\varepsilon_s = 0$ (bottom) with 56708 finite elements

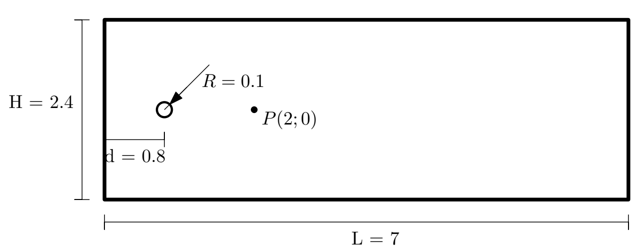


Figure 9: Flow around a cylinder: computational domain

*Monophase case.* Following [27], we considered $\rho_g = 1$ kg/m$^3$, $T = 9.73\,10^{-3}$ K, and $u_1 = u_2 = 0$ m/s as the initial conditions of the whole domain. The inlet condition is placed on the left side of the domain and it consists of a velocity of $u_{in} = 1$ m/s, a gas density $\rho_g = 1$ kg/m$^3$, and a temperature $T = 9.73\,10^{-3}$ K. Since the flow is at a subsonic regime, an output boundary condition is required, therefore we set the gas density to $\rho_g = 1$ kg/m$^3$ at the right side of the domain. On the upper and lower sides of the domain, a slip condition is imposed, whereas a no-slip condition is imposed on the boundary of the cylinder. The gas viscosity is set to 0.002 kg/m s and the thermal diffusivity is 2.8676 W/m K. These coefficients determine, together with the dimensions of the problem and the values of the inlet boundary conditions, a monophase compressible flow with a Reynolds number $Re = 100$ and a Mach number $Ma = 0.5$.

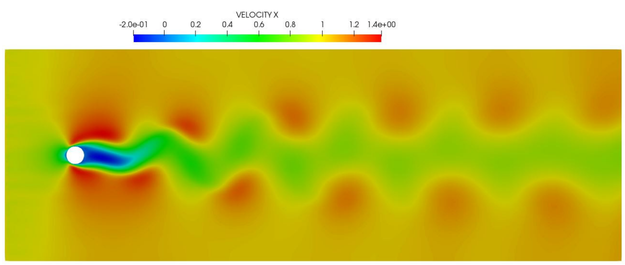


Figure 10: Monophase flow around a cylinder: horizontal velocity field at $t = 30$ s.

In Figure 10, we show the velocity field at $t = 30$ s when the vortices behind the cylinder are clearly visible.

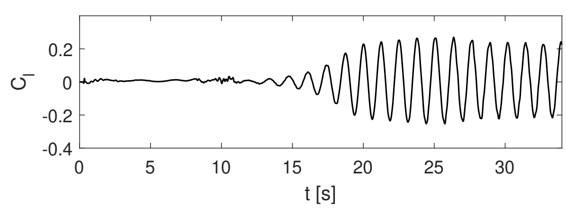


Figure 11: Monophase flow around a cylinder: lift coefficient versus time.

In Figure 11, we show the trend of the lift coefficient $C_l$, computed as

$$C_l = \frac{\int_\Gamma (-p\mathbf{I} + \boldsymbol{\tau}) \cdot \mathbf{n} d\Gamma}{\frac{1}{2}\rho_{in} u_{in}^2 D} \tag{51}$$

versus time, being $\Gamma$ the boundary of the cylinder. The lift coefficient begins to oscillate around zero after about 15 s, with an amplitude that, at regime, is of about 0.25, comparable with the results shown in [27]. The frequency of the oscillations $f_f$ of the lift coefficient is also comparable to the one obtained in [27]. In the present work, we obtain $f_f \simeq 0.85$, whereas in [27] the reference value is $f_f = 0.91$. The slight discrepancy may be due to the use of different time integration methods and finite element meshes.

*Biphase case.* We repeat the simulation for the same initial conditions (absence of solid particulate on the whole domain), and an impulsive inlet condition for the solid phase concentration, that is set to $\varepsilon_s = 10^{-4}$ after the first time step. In this simulation, the Reynolds number and the compressibility regime evolve during the analysis, according to Equations (11) and (22), therefore we cannot provide unique Reynolds and Mach numbers for this problem.

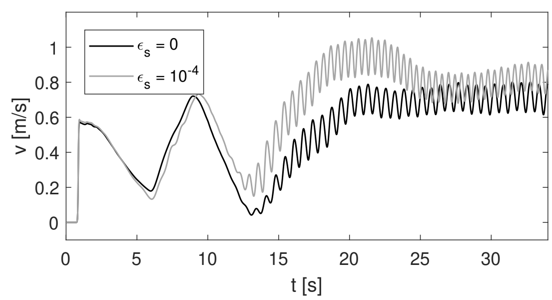


Figure 12: Flow around a cylinder: horizontal velocity field at the point $P(2;0)$ for the monophase case and the multiphase case with $\varepsilon_s = 10^{-4}$.

In Figure 12, we show the time evolution of the velocity field computed at the point $P(2,0)$ and obtained for the monophase and two-phase flows. We notice that the two plots are similar in the first part of the graph, because, during the first phase of the analysis, the solid concentration has not yet reached the point $P$, and the flow is practically monophase. Later, once the particle wave reaches the sample point $P$, the two curves diverge. ~~progressively.~~

In Figure 13, we show the horizontal velocity and the solid concentration fields at $t = 30s$. Comparing Figure 13b and Figure 10, we observe that the multiphase case gives higher velocities with respect to the monophase case.

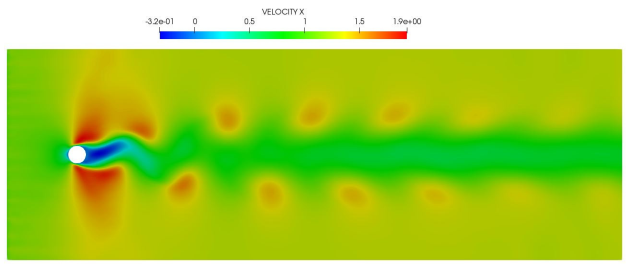


(a) Velocity field

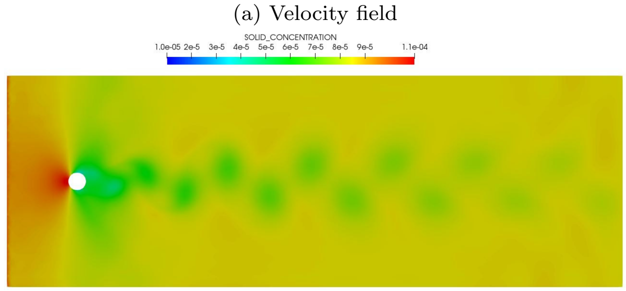


(b) Solid concentration field

Figure 13: Biphase flow around a cylinder: velocity and solid concentration fields at $t = 30$ s

### *4.4. A real case application: pyroclastic flow against buildings*

In this section, we present the application of the proposed formulation to the simulation of a pyroclastic gravity current, a multiphase flow composed by a mixture of gas and solid particulates, originated from the fragmentation of magma after a volcanic event. Assuming that the gas phase is composed by only air ($\mu_g = 2 \cdot 10^{-5}$ kg/m s, $c_p = 1010$ J/kg K, $\lambda_g = 0.026$ W/m K), and considering a solid phase composed by particles of diameter 190 $\mu$m [9] and density $\rho_s = 1800$ kg/m$^3$, we obtain the characteristic times $\tau_u = 0.36$ s (see Equation (6)) and $\tau_T = 0.21$ s (see Equation (7)). We analyze the effects of the volcanic event over a urban settlement placed at a distance of 5 km from the crater of the volcano, thus at a distance such that the characteristic times are abundantly overcome. This allows us to consider that the hypothesis of thermal and kinetic equilibrium is fulfilled, and to use Equations (8)-(9) for the problem solution.

The computational domain, shown in Figure 14, consists of a rectangular domain of 1 km in length and 200 m in height, with two obstacles representing two buildings, the first one (20 m high) located at 150 m from the inlet (at the left side of the domain), and the second one (50 m high) placed at a

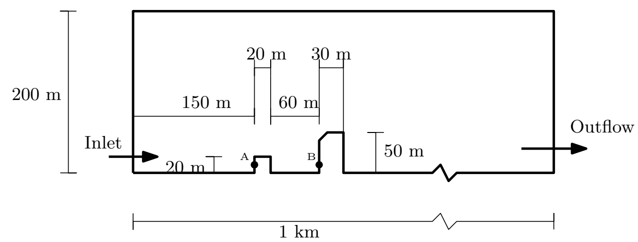


Figure 14: Pyroclastic flow simulation: computational domain.

distance of 60 m from the first building.

The length and the height of the computational domain have been chosen such that the pyroclastic flow does not alter the variables in correspondence of the outflow and the upper part of the domain.

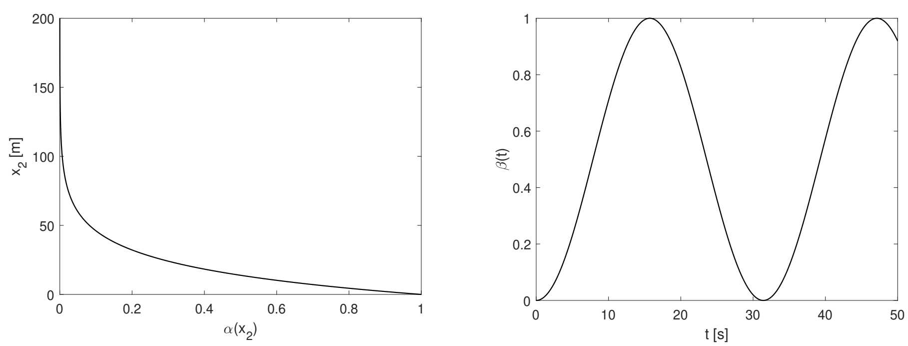


(a) $\alpha(x_2)$ (b) $\beta(t)$

Figure 15: Plot of function $\alpha(x_2)$ and $\beta(t)$ used for the inlet of the pyroclastic flow simulation

The initial conditions are coherent with a situation of stationary air at 300 K. The initial density of the gas is set to $\rho_g = 1.225$ kg/m$^3$. At the inlet a time-varying boundary condition is imposed, that is

$$
\begin{aligned}
\varepsilon_s(x_1 = 0, x_2, t) &= \varepsilon_{s,max}\alpha(x_2)\beta(t) \\
u_1(x_1 = 0, x_2, t) &= u_{1,max}\alpha(x_2)\beta(t) \\
u_2(x_1 = 0, x_2, t) &= 0\,\mathrm{m/s} \\
T(x_1 = 0, x_2, t) &= 300 \ \mathrm{K}
\end{aligned}
\tag{52}
$$

where $\varepsilon_{s,max} = 5 \cdot 10^{-3}$, $u_{1,max} = 60$ m/s. $\alpha(x_2)$ and $\beta(t)$ are functions describing the spatial and temporal profiles of the inlet conditions, defined as

$$
\begin{aligned}
\alpha(x_2) &= \exp\left(-\frac{x_2}{20}\right) \\
\beta(t) &= \frac{1}{2}\left(1-\cos\left(\frac{t}{5}\right)\right)
\end{aligned}
\tag{53}
$$

and represented in Figure 15.

The spatial exponential function $\alpha(x_2)$ models a distribution that is larger in the proximity of the ground and vanishes at high altitudes, coherently with the results presented in [9]. On the other hand, the time function $\beta(t)$ allows us to reproduce subsequent waves of pyroclastic material. The gravitational load is modeled as a field load $g = -9.81$ m/s$^2$ in the direction of the vertical axis.

The simulation is run for a total time duration of 50 s.

In Figure 16, we show the concentration of the solid phase at different time instants.

Figure 17 shows the velocity vectors diagram obtained at $t = 24$ s in the part of domain comprised between the two obstacles. The formation of a vortex between the two obstacles can be clearly appreciated from the picture. Figure 18 shows the pressure distribution on the domain for the same time instant.

We repeat the simulation for a less dense mixture ($\varepsilon_{s,max} = 1 \cdot 10^{-3}$) with the aim of comparing the pressure fields over the civil buildings given by the two different pyroclastic flow scenarios.

In Figure 19, we show the diagram of the pressure versus time computed at the two sample points $A$ and $B$ of Figure 14 for the two different values of the inlet concentrations $\varepsilon_{s,max}$. Initially, the time evolution of the pressure value at points $A$ and $B$ is the same for both solid concentrations.

As the gravity current reaches the first building (at around $t = 10$ s), the solutions start to diverge. In particular, the pressure at point $A$ increases sensibly for both $\varepsilon_{s,max} = 1 \cdot 10^{-3}$ and $\varepsilon_{s,max} = 5 \cdot 10^{-3}$ while it does not vary significantly for point $B$ (hydrostatic value). At about $t = 18$ s, the pressure in the point $B$ increases for the case $\varepsilon_{s,max} = 5 \cdot 10^{-3}$ since the mixture overcomes the first obstacle and hits the second one; for the case $\varepsilon_{s,max} = 1 \cdot 10^{-3}$, on the contrary, the amount of material overcoming the first obstacle is minor, and the increase of pressure in $B$ happens later, and

(a) 8 s

(b) 16 s

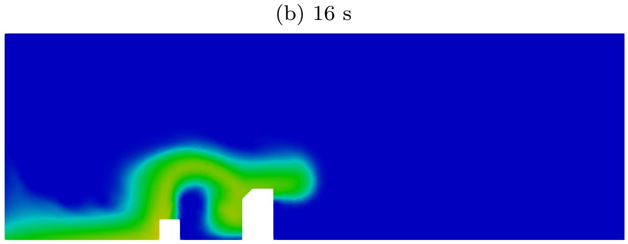

(c) 24 s

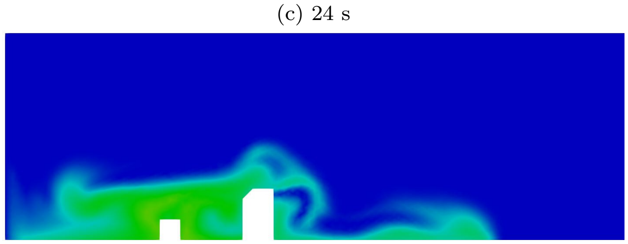

(d) 32 s


Figure 16: Pyroclastic flow simulation: solid concentration at different time instants

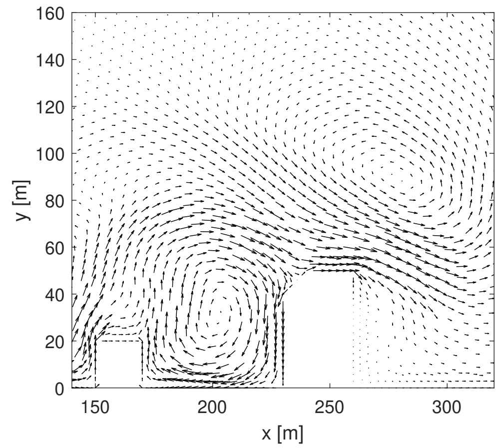


Figure 17: Pyroclastic flow simulation: velocity diagram at $t = 24$ s

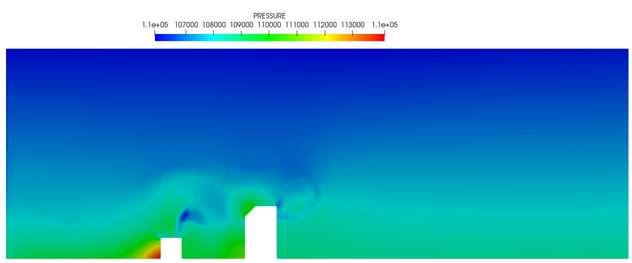


Figure 18: Pyroclastic flow simulation: pressure field at $t = 24$ s.

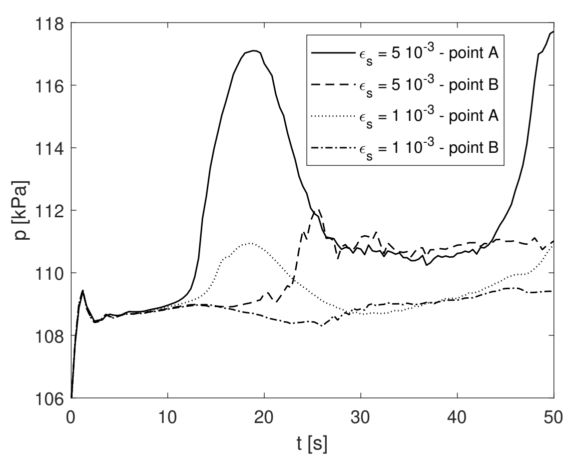


Figure 19: Pyroclastic flow simulation: pressure at points $A$ and $B$ for different values of the maximum concentration of the solid phase.

with less intensity. These pressure results show clearly the barrier effect produced by those buildings of the urban settlement that are most exposed to the pyroclastic gravity current.

Basing on the classification proposed in [4] to correlate different levels of damage on civil constructions with the dynamic pressure acting on them, we have estimated the damages produced by the pyroclastic flow over the two buildings considered in this test case. In particular, we have evaluated the overpressure values with respect to the hydrostatic ones from the pressure solution obtained at the façades of the two buildings. For the case of solid concentration $\varepsilon_{s,max} = 5 \cdot 10^{-3}$, the overpressure reaches 9 kPa in the first building, while it is only 3 kPa in the second building. The lower value of overpressure on the second building is attributable to the barrier effect produced by the first one. In terms of damages, these pressure values would lead to heavy damages for the first building and light/moderate ones for the second construction, according to [4]. On the other hand, for the case of solid concentration $\varepsilon_{s,max} = 1 \cdot 10^{-3}$, the overpressure is almost always below the value of 2 kPa, which corresponds to light damages.

### *4.5. Real-scale application*

In this test, we analyze the impact of a realistic pyroclastic flow impacting a urban settlement considering a large-scale three-dimensional (3D) geometry. Ten buildings of height of 30 m are distributed over a rectangular plan of sides $L = 600$ m and $W = 100$ m. A maximum height $H = 200$ m is considered for the external environment. 3D and planar views of the computational domain are provided in Figure 20.

Slip boundary conditions are considered on the ground, on the lateral surfaces of the domain, and on the external boundaries of the buildings. The following inlet condition is applied on the rectangular surface placed at $x = 0$:

$$
\begin{aligned}
\varepsilon_s(x=0,y,z,t) &= \varepsilon_{s,max} e^{-z/20}(1-e^{-t}) \\
u_1(x=0,y,z,t) &= u_{1,max}\, e^{-z/100}(1-e^{-t}) \\
u_2(x=0,y,z,t) &= 0\,\mathrm{m/s} \\
u_3(x=0,y,z,t) &= 0\,\mathrm{m/s} \\
T(x=0,y,z,t) &= T_0(1-k\,z)
\end{aligned}
\tag{54}
$$

with $\varepsilon_{s,max} = 10^{-2}$, $u_{1,max} = 30$ m/s, $T_0 = 300$ K, and $k = 0.01$ m$^{-1}$. The solid density $\rho_s$ is set to $2.8\,10^3$ kg/m$^3$.

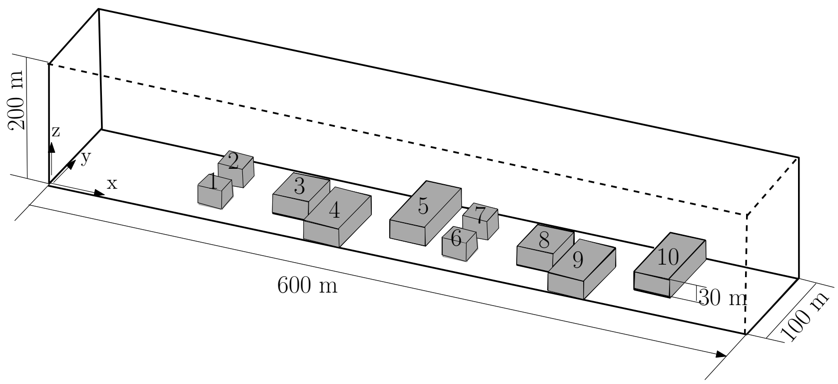


(a) Three-dimensional view

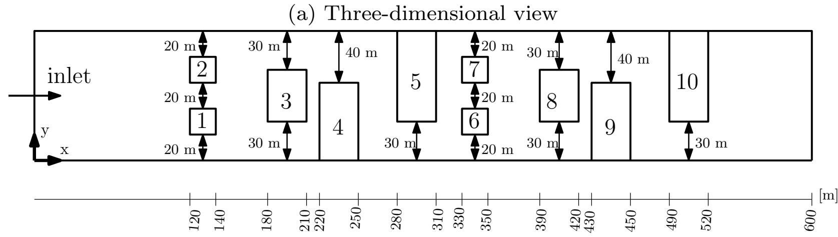


(b) Plan

Figure 20: Computational domain of the 3d real scale application

As initial condition, we consider zero velocity and zero solid particle concentration in the whole domain. In order to avoid unphysical velocities at the top of the computational domain, we also consider two functions of the sole variable $z$ as initial conditions for the density and the temperature. These functions satisfy at the same time the stationary version of Equations (8b), (8c), and the equation of state for gas (4), under the constraints of zero velocity.

Assuming a linear variation along the $z$-axis for the initial temperature field [53], such that

$$T(z) = T_0(1 - k\, z), \tag{55}$$

the initial condition for the gas density is found by solving

$$\frac{\partial}{\partial z}[\rho R T_0(1 - kz)] + \rho g = 0 \tag{56a}$$

$$\rho(z = 0) = \rho_0 \tag{56b}$$

$\rho_0$ being the density at the ground level and at atmospheric standard conditions.

The domain has been discretized with a finite elements mesh of 940785 linear tetrahedra with mean size of 5 m, giving an overall amount of 168841 nodes.

Following the standard practice for this natural hazard scenario [12, 54], we measure the impact of the pyroclastic flow in terms of the dynamic pressure, which is computed as $p_{dyn} = 0.5\rho\|\mathbf{u}\|^2$. This value is measured for each building at the geometrical center of its façade closest to the inlet.

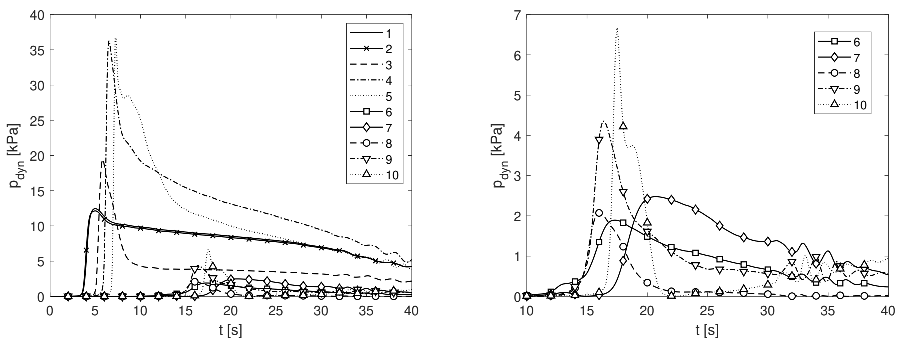


(a) Global view

(b) Zoom on the curves of buildings 6-10

Figure 21: Real scale application: dynamic pressure on buildings

The graphs of Figure 21 show the time evolution of the dynamic pressure at the ten buildings. Despite the differences in magnitude, all the curves show an initial peak followed by a relatively sudden decrease. Due to symmetry, the curves of buildings 1 and 2 are practically superimposed. However, for the rest of buildings, this symmetrical behavior is lost due to their asymmetrical distribution. This is clearly shown by the response of buildings 6 and 7, which, although they have the same relative position as buildings 1 and 2, give rise to totally different pressure curves (see Figure 21b).

The most noticeable finding is that buildings 6-10 exhibit a first peak of dynamic pressure much lower than the one of buildings 1-5. In particular, the highest peaks in the first set of buildings is obtained on buildings 4 and 5. These results show clearly the shielding effect produced by the buildings closest to the pyroclastic flow sources. Indeed, the first set of building retains and slows down the pyroclastic material and this makes reducing the flow density and velocity, and so the overall dangerousness of the pyroclastic flow.

Analogously to what done for the previous test, we have analysed the potential damages over the buildings basing on the criteria given in [4]. In

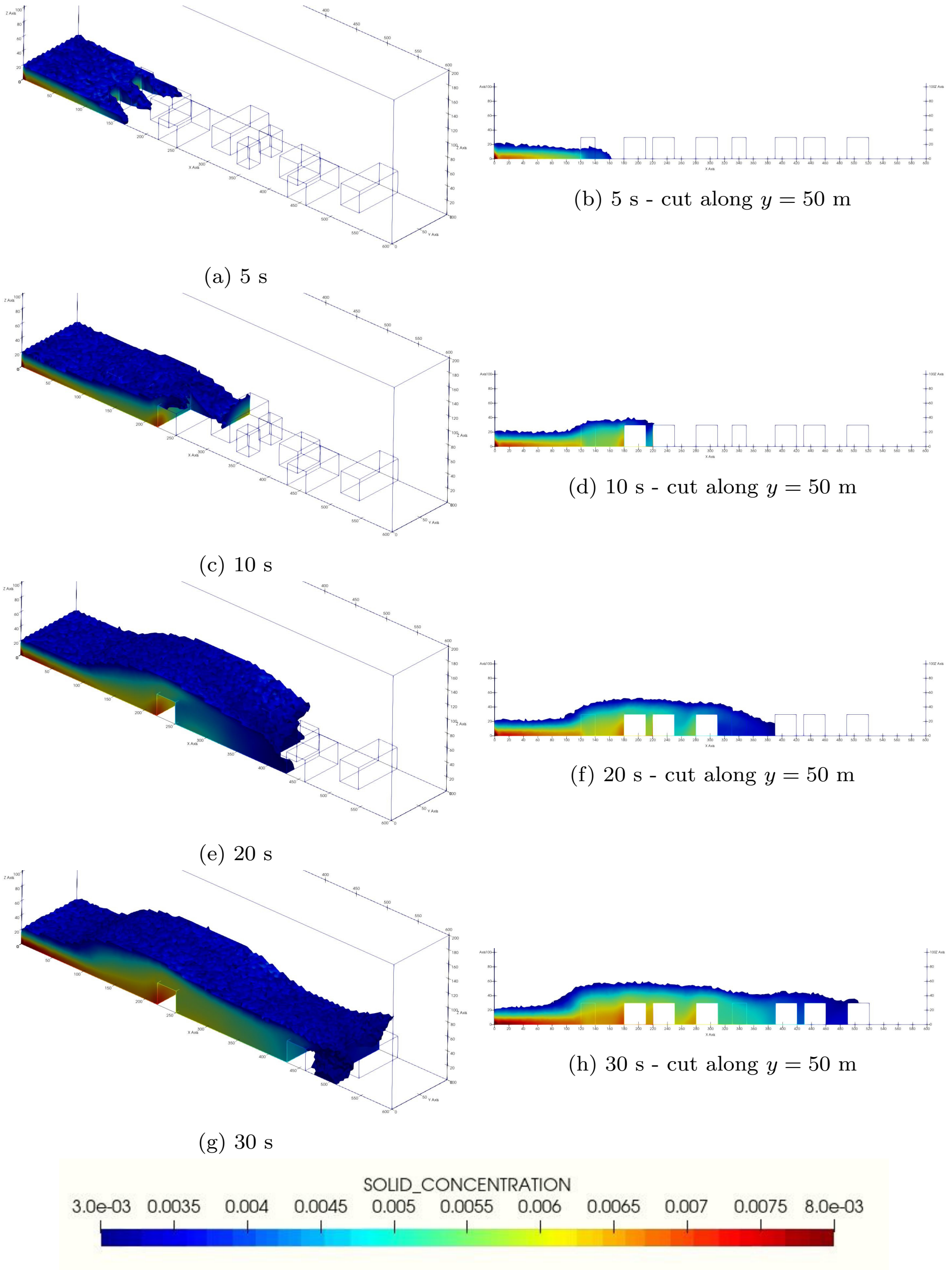


(a) 5 s

(b) 5 s - cut along $y = 50$ m

(c) 10 s

(d) 10 s - cut along $y = 50$ m

(e) 20 s

(f) 20 s - cut along $y = 50$ m

(g) 30 s

(h) 30 s - cut along $y = 50$ m

Figure 22: Three-dimensional simulation: solid concentration at different time instants (the values lower than $\varepsilon_s = 3 \cdot 10^{-3}$ are not represented). Left column: Three dimensional view; right column: cut view at $y = 50$ m.

this case, the peaks of dynamic pressure measured at buildings 4 and 5 would lead to a *total devastation* of the structures, meaning that walls would be completely destroyed and washed out. The other buildings of the first group (buildings 1, 2, 3) would also undergo severe damages (*partial devastation* according to [4]), while the buildings of the second group would suffer from moderate damages. A color map of the level of damage in accordance with this classification is reported in Figure 23.

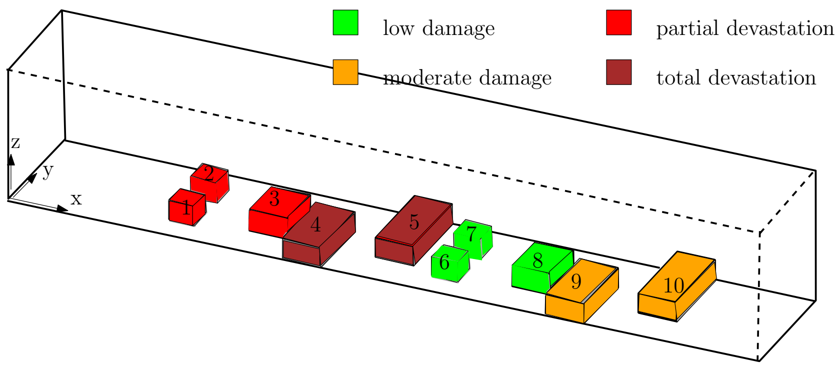


Figure 23: Three-dimensional simulation: simulated level of damage for each building.

The solution in terms of the solid material concentration obtained at four different time instants is plotted in Figure 22. Figures 22a-22b show the advancement of the flow at $t = 5s$. At this moment, the solid particulate is flowing around buildings 1-2, following three different channels in a symmetrical way. At $t = 10s$, as shown in Figures 22c-22d, the flow has already overcome buildings 1-3, and, after surrounding building 4, has impacted against building 5. At $t = 20s$ (Figures 22e-22f), the pyroclastic current has already reached building 9, and finally, in Figures 22g-22h, the flow is overcoming also building 10.

Figure 22 also shows that the the highest concentration of pyroclastic material is retained by the first set of buildings, remarking again the above-mentioned shielding effects.

In order to assess the stability and smoothness of the pressure field, in Figure 24 we show the pressure distribution on the plan $x_2 = 50$ m. The pressure results confirm the validity of the proposed stabilized formulation, since no instabilities are exhibited.

To conclude, this numerical test shows the applicability of the proposed explicit multiphase formulation to demanding computations of pyroclastic

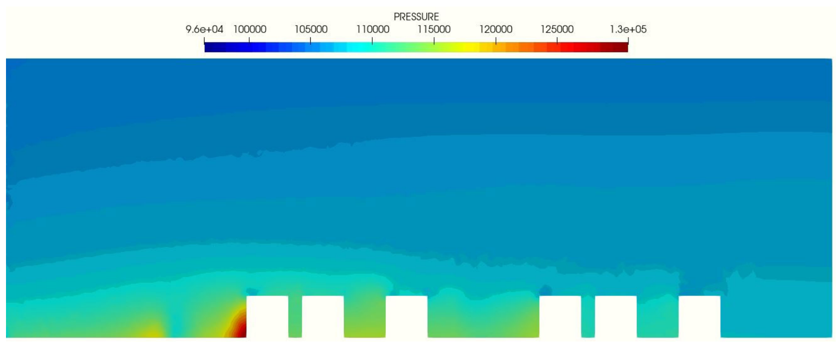

Figure 24: Three-dimensional simulation: pressure distribution at $t = 20$ s, for $y = 50$ m.

gravity currents on urban settlements and its suitability for risk assessment studies.

## 5. Conclusion

In this work, we extend the stabilized finite element formulation proposed for compressible monophase flows to multiphase mixtures composed of a compressible fluid and a dilute solid phase. In particular, we investigate the case of compressible multiphase flows in kinetic and thermic equilibrium, for which a unique velocity and temperature field can be assumed for all the mixture components. This situation is representative of pyroclastic flows considered at a certain distance from a volcanic eruption source.

Given the formal similarities between the formulation for a compressible monophase flow and a multiphase flow, we adopt the same stabilization strategies as those used in the literature for the monophase compressible case. In particular, we use the Variational Multiscale Method for the stabilization of the convective part, and an isotropic discontinuity capturing technique for dealing with the eventual discontinuities.

The robustness of the approach has been tested on several benchmarks proposed in the literature, and here slightly modified to introduce multiphase examples. The results confirm the accuracy and robustness of the formulation for monophase compressible problems and show also its validity for multiphase problems.

Finally, we applied the proposed stabilized formulation to the study of the dynamics of pyroclastic flows impacting against buildings, an application of interest for the evaluation of the risk in case of volcanic eruptive events.

We first analyzed a two-dimensional case considering pyroclastic flows with different solid concentrations. Then, we applied the numerical method to the solution of a large-scale problem in three dimensions. Basing on the damages classifications proposed by [4], we also quantified the potential damages over the civil constructions produced by the impact of the pyroclastic flow. These results proved the suitability of the proposed technique for the study of real-world scenarios of pyroclastic flows.

Future developments of this work will include analyses of the sensitivity of the model with respect to the involved physical parameters, as well as the evaluation of the barrier effect of the buildings depending on the geometrical characteristics of the urban settlement. From the numerical point of view, future work will be the coupling of the present Eulerian formulation with Lagrangian approaches, such as the Discrete Element Method (DEM), for the simulation of particles in suspension for case in which the hypotheses of kinetic and thermal equilibrium are not applicable.

## Appendix A. Appendix

Here we report the steps to bring Equation (38) to its semidiscrete form (44). Introducing (43) we get

$$\begin{aligned}
&\hat{V}_s^h \int_{\Omega_h} N_{is} N_{ip} d\Omega \frac{\partial}{\partial t} \hat{U}_p^h + \hat{V}_s^h \int_{\Omega_h} A_{ijk}(\mathbf{U}^h) D_{kpj} d\Omega \hat{U}_p^h - \hat{V}_s^h \int_{\Omega_h} T_{ik} N_{kp} d\Omega \hat{U}_p^h \\
&-\hat{V}_s^h \int_{\Omega_h} \left( D_{isj} A_{ijk}(\mathbf{U}^h) + N_{is} B_{ijkm}(\mathbf{U}^h) \frac{\partial U_m^h}{\partial x_j} - N_{is} T_{sk} \tau_{kj} N_{jp} \right) d\Omega \hat{R}_p^h + \\
&\hat{V}_s^h \int_{\Omega_h} \left( D_{isj} G_{ij}(\mathbf{U}^h) d\Omega_h \right) d\Omega = 0
\end{aligned} \tag{A.1}$$

where $\Omega_h$ is the domain of the finite element and matrix $\mathbf{D}$ containing the derivatives of the shape functions is defined as

$$D_{ijk} = \frac{\partial N_{ij}}{x_k} \tag{A.2}$$

Since Equation (A.1) holds for every choice of the test function $\hat{V}_s^h$, then

$$M_{sp} \frac{\partial}{\partial t} \hat{U}_p^h = \hat{F}_s \tag{A.3}$$

also holds, where

$$M_{sp} = \int_{\Omega_h} N_{is} N_{ip} d\Omega$$

$$\hat{F}_s = -\int_{\Omega_h} A_{ijk}(\mathbf{U}^h) D_{kpj} d\Omega \hat{U}_p^h + \int_{\Omega_h} T_{ik} N_{kp} d\Omega \hat{U}_p^h +$$

$$+ \int_{\Omega_h} \left( D_{isj} A_{ijk}(\mathbf{U}^h) + N_{is} B_{ijkm}(\mathbf{U}^h) \frac{\partial U_m^h}{\partial x_j} - N_{is} T_{sk} \tau_{kj} N_{jp} \right) d\Omega \hat{R}_p^h +$$

$$- \int_{\Omega_h} \big( D_{isj} G_{ij}(\mathbf{U}^h) d\Omega_h \big) \tag{A.4}$$

$M_{sp}$ is the consistent mass matrix, and, in view of an explicit algorithm for the time integration, can be lumped, bringing to the final semidiscrete form (44).

## Acknowledgements

This work is partially funded by the Italian Ministry of University and Research (MUR) through the project PON-AIM "Attraction and International Mobility" CUP: E66C19000230005, and partially funded by the Spanish Ministry of Economy and Competitiveness (Ministerio de Economia y Competitividad, MINECO) through the project PRECISE (BIA2017- 83805-R).

Authors are also grateful to the CINECA consortium for the provision of computational utilities through the IsCRA project "Vulnerability and Risk Assessment" (IsC79-VRA).

## References

[1] R. V. Fisher, Models for pyroclastic surges and pyroclastic flows, Journal of Volcanology and Geothermal Research 6 (1979) 305–318.

[2] J. V. Wright, A. L. Smith, S. Self, A working terminology of pyroclastic deposits, Journal of Volcanology and Geothermal Research 8 (1980) 315–336.

[3] G. Zuccaro, F. Cacace, R. Spence, P. Baxter, Impact of explosive eruption scenarios at vesuvius, Journal of Volcanology and Geothermal Research 178 (2008) 416–453.

[4] P. J. Baxter, R. Boyle, P. Cole, A. Neri, R. Spence, G. Zuccaro, The impacts of pyroclastic surges on buildings at the eruption of the soufrière hills volcano, montserrat, Bulletin of volcanology 67 (2005) 292–313.

[5] G. Zuccaro, D. De Gregorio, Impact assessments in volcanic areas-the vesuvius and campi flegrei cases studies, Annals of Geophysics 62 (2019) 02.

[6] G. Zuccaro, M. F. Leone, Building technologies for the mitigation of volcanic risk: Vesuvius and campi flegrei, Natural hazards review 13 (2012) 221–232.

[7] R. J. Spence, G. Zuccaro, S. Petrazzuoli, P. J. Baxter, Resistance of buildings to pyroclastic flows: analytical and experimental studies and their application to vesuvius, Natural Hazards Review 5 (2004) 48–59.

[8] D. Gidaspow, Multiphase flow and fluidization: continuum and kinetic theory descriptions, Academic press, 1994.

[9] A. Neri, T. Esposti Ongaro, G. Macedonio, D. Gidaspow, Multiparticle simulation of collapsing volcanic columns and pyroclastic flow, Journal of Geophysical Research: Solid Earth 108 (2003).

[10] T. Esposti Ongaro, C. Cavazzoni, G. Erbacci, A. Neri, M.-V. Salvetti, A parallel multiphase flow code for the 3d simulation of explosive volcanic eruptions, Parallel Computing 33 (2007) 541–560.

[11] M. Pelanti, R. J. LeVeque, High-resolution finite volume methods for dusty gas jets and plumes, SIAM Journal on Scientific Computing 28 (2006) 1335–1360.

[12] G. Zuccaro, D. Ianniello, Interaction of pyroclastic flows with building structures in an urban settlement: a fluid-dynamic simulation impact

model, Journal of volcanology and geothermal research 133 (2004) 345–352.

[13] P. Dellino, D. Mele, R. Sulpizio, L. La Volpe, G. Braia, A method for the calculation of the impact parameters of dilute pyroclastic density currents based on deposit particle characteristics, Journal of Geophysical Research: Solid Earth 113 (2008).

[14] R. Sulpizio, P. Dellino, D. Doronzo, D. Sarocchi, Pyroclastic density currents: state of the art and perspectives, Journal of Volcanology and Geothermal Research 283 (2014) 36–65.

[15] M. Cerminara, T. Esposti Ongaro, L. C. Berselli, Ashee-1.0: a compressible, equilibrium–eulerian model for volcanic ash plumes, Geoscientific Model Development 9 (2016) 697–730.

[16] L. P. Franca, S. L. Frey, T. J. Hughes, Stabilized finite element methods: I. application to the advective-diffusive model, Computer Methods in Applied Mechanics and Engineering 95 (1992) 253–276.

[17] I. Harari, T. J. Hughes, Stabilized finite element methods for steady advection—diffusion with production, Computer Methods in Applied Mechanics and Engineering 115 (1994) 165–191.

[18] R. Codina, Stabilized finite element approximation of transient incompressible flows using orthogonal subscales, Computer methods in applied mechanics and engineering 191 (2002) 4295–4321.

[19] T. Tezduyar, T. Hughes, Finite element formulations for convection dominated flows with particular emphasis on the compressible euler equations, in: 21st Aerospace Sciences Meeting, 1983, p. 125.

[20] M. Polner, Galerkin Least-Squares stabilization operators for the Navier-Stokes equations, Ph.D. thesis, PhD thesis, University of Twente, 2005.

[21] F. Shakib, Finite element analysis of the compressible euler and navier-stokes equations (1989).

[22] T. J. Hughes, G. R. Feijóo, L. Mazzei, J.-B. Quincy, The variational multiscale method—a paradigm for computational mechanics, Computer methods in applied mechanics and engineering 166 (1998) 3–24.

[23] T. J. Hughes, Multiscale phenomena: Green's functions, the dirichlet-to-neumann formulation, subgrid scale models, bubbles and the origins of stabilized methods, Computer methods in applied mechanics and engineering 127 (1995) 387–401.

[24] Y. Bazilevs, V. Calo, J. Cottrell, T. Hughes, A. Reali, G. Scovazzi, Variational multiscale residual-based turbulence modeling for large eddy simulation of incompressible flows, Computer methods in applied mechanics and engineering 197 (2007) 173–201.

[25] N. Ahmed, T. C. Rebollo, V. John, S. Rubino, A review of variational multiscale methods for the simulation of turbulent incompressible flows, Archives of Computational Methods in Engineering 24 (2017) 115–164.

[26] B. Koobus, C. Farhat, A variational multiscale method for the large eddy simulation of compressible turbulent flows on unstructured meshes—-application to vortex shedding, Computer Methods in Applied Mechanics and Engineering 193 (2004) 1367–1383.

[27] C. A. Bayona Roa, J. Baiges, R. Codina, Variational multi-scale finite element approximation of the compressible navier-stokes equations, International Journal of Numerical Methods for Heat & Fluid Flow (2016).

[28] M. Avila, J. Principe, R. Codina, A finite element dynamical nonlinear subscale approximation for the low mach number flow equations, Journal of Computational Physics 230 (2011) 7988–8009.

[29] C. Bayona Roa, J. Baiges, R. Codina, Variational multiscale approximation of the one-dimensional forced burgers equation: The role of orthogonal subgrid scales in turbulence modeling, International Journal for Numerical Methods in Fluids 86 (2018) 313–328.

[30] R. Codina, Stabilization of incompressibility and convection through orthogonal sub-scales in finite element methods, Computer methods in applied mechanics and engineering 190 (2000) 1579–1599.

[31] T. E. Tezduyar, Y. Park, Discontinuity-capturing finite element formulations for nonlinear convection-diffusion-reaction equations, Computer methods in applied mechanics and engineering 59 (1986) 307–325.

[32] F. Rispoli, A. Corsini, T. E. Tezduyar, Finite element computation of turbulent flows with the discontinuity-capturing directional dissipation (dcdd), Computers & fluids 36 (2007) 121–126.

[33] T. E. Tezduyar, M. Senga, Stabilization and shock-capturing parameters in supg formulation of compressible flows, Computer methods in applied mechanics and engineering 195 (2006) 1621–1632.

[34] M. R. Baer, J. W. Nunziato, A two-phase mixture theory for the deflagration-to-detonation transition (ddt) in reactive granular materials, International journal of multiphase flow 12 (1986) 861–889.

[35] A. Kapila, R. Menikoff, J. Bdzil, S. Son, D. S. Stewart, Two-phase modeling of deflagration-to-detonation transition in granular materials: Reduced equations, Physics of fluids 13 (2001) 3002–3024.

[36] N. Andrianov, G. Warnecke, The riemann problem for the baer–nunziato two-phase flow model, Journal of Computational Physics 195 (2004) 434–464.

[37] A. Murrone, H. Guillard, A five equation reduced model for compressible two phase flow problems, Journal of Computational Physics 202 (2005) 664–698.

[38] D. W. Schwendeman, C. W. Wahle, A. K. Kapila, The riemann problem and a high-resolution godunov method for a model of compressible two-phase flow, Journal of Computational Physics 212 (2006) 490–526.

[39] M. Dumbser, A diffuse interface method for complex three-dimensional free surface flows, Computer Methods in Applied Mechanics and Engineering 257 (2013) 47–64.

[40] F. Kemm, E. Gaburro, F. Thein, M. Dumbser, A simple diffuse interface approach for compressible flows around moving solids of arbitrary shape based on a reduced baer–nunziato model, Computers & Fluids 204 (2020) 104536.

[41] R. Saurel, R. Abgrall, A multiphase godunov method for compressible multifluid and multiphase flows, Journal of Computational Physics 150 (1999) 425–467.

[42] F. E. Marble, Dynamics of dusty gases, Annual Review of Fluid Mechanics 2 (1970) 397–446.

[43] S. Carcano, T. E. Ongaro, L. Bonaventura, A. Neri, Influence of grain-size distribution on the dynamics of underexpanded volcanic jets, Journal of volcanology and geothermal research 285 (2014) 60–80.

[44] R. Codina, A discontinuity-capturing crosswind-dissipation for the finite element solution of the convection-diffusion equation, Computer Methods in Applied Mechanics and Engineering 110 (1993) 325–342.

[45] P. Dadvand, R. Rossi, E. Oñate, An object-oriented environment for developing finite element codes for multi-disciplinary applications, Archives of computational methods in engineering 17 (2010) 253–297.

[46] G. I. Taylor, A. E. Green, Mechanism of the production of small eddies from large ones, Proceedings of the Royal Society of London. Series A-Mathematical and Physical Sciences 158 (1937) 499–521.

[47] G. A. Sod, A survey of several finite difference methods for systems of nonlinear hyperbolic conservation laws, Journal of computational physics 27 (1978) 1–31.

[48] L. Catabriga, D. A. de Souza, A. L. Coutinho, T. E. Tezduyar, Three-dimensional edge-based supg computation of inviscid compressible flows with yz$\beta$ shock-capturing, Journal of Applied Mechanics 76 (2009).

[49] S. Clain, S. Diot, R. Loubère, A high-order finite volume method for systems of conservation laws—multi-dimensional optimal order detection (mood), Journal of computational Physics 230 (2011) 4028–4050.

[50] L. Fu, A low-dissipation finite-volume method based on a new teno shock-capturing scheme, Computer Physics Communications 235 (2019) 25–39.

[51] M. Cremonesi, A. Frangi, A lagrangian finite element method for 3d compressible flow applications, Computer Methods in Applied Mechanics and Engineering 311 (2016) 374–392.

[52] E. F. Toro, Riemann solvers and numerical methods for fluid dynamics: a practical introduction, Springer Science & Business Media, 2013.

[53] M. Pidwirny, The Layered Atmosphere - Fundamentals of Physical Geography, 2nd ed., National Council of Educational Research and Training, 2006.

[54] P. Dellino, F. Dioguardi, R. Isaia, R. Sulpizio, D. Mele, The impact of pyroclastic density currents duration on humans: the case of the ad 79 eruption of vesuvius, Scientific Reports 11 (2021) 1–9.